**RESEARCH ARTICLE**

# Fault Diagnosis Scheme for Open-Circuit Fault in N+2 Converter of Six-Phase SRM Using Midpoint Current Spectrum Analysis

**MINJUN GUAN[1], CHUANG LIU[2], PEILIN LIU[2],
AND XIAODONG SUN[3], (Senior Member, IEEE)**

[1]College of Mechanical and Electrical Engineering, Jinling Institute of Technology, Nanjing 211169, China
[2]College of Automation Engineering, Nanjing University of Aeronautics and Astronautics, Nanjing 211106, China
[3]Automotive Engineering Research Institute, Jiangsu University, Zhenjiang 212013, China

Corresponding author: Minjun Guan (gmj_wsxaa@foxmail.com)

**ABSTRACT** In this paper, a six-phase N+2 power converter for switched reluctance motor is studied. An open-circuit fault diagnosis and faulty devices location scheme based on midpoint current spectrum analysis is proposed. In order to realize fault diagnosis, five fault cases are distinguished, including single-phase fault, multiphase fault and midpoint switch fault. Taking the phase current frequency as the fundamental frequency, the DC component, the fundamental frequency component, and the second harmonic component have different change rules in the five fault cases. The third harmonic component is used as the denominator, three spectrum coefficient could be obtained and be used as the fault characteristic. Through this scheme, using a single current sensor to detect the midpoint current can ensure open-circuit faults accurately. After the fault case is confirmed, the amplitude of the harmonic component is used to define a fault location threshold, and the threshold is numerically compared with the midpoint current to realize the faulty bridge arm location. Finally, the complete process of fault diagnosis and location is described, then the effectiveness of the proposed diagnosis method is validated by the simulation and experiment.

**INDEX TERMS** Switched reluctance motor (SRM), power converter, fault diagnosis, spectrum analysis.

## I. INTRODUCTION

With the development of electric vehicles, new energy power generation, aerospace technology, and so on, there is an increasing demand for motor systems with larger capacity, higher reliability and better fault tolerance. Switch Reluctance Motors (SRMs) have some distinct features including simple structure, permanent magnet material needless, these characteristics make SRMs have prominent advantages in some applications requiring low cost, high reliability and wide speed range [1], [2], [3].

However, SRMs also have obvious disadvantages such as high torque ripple, high vibration noise, and low power density [4], [5], [6]. Furthermore, the most widely used

The associate editor coordinating the review of this manuscript and approving it for publication was Christopher H. T. Lee.

power converter in SRM drive systems is the Asymmetric Half Bridge (AHB) converter, three-phase full-bridge power converters cannot be used directly [7]. Hence, novel converter topology with high performance has also received a lot of attention in the SRM research field [8], [9].

For some applications, increase the phase number is a simple and effective method to decrease the torque ripple and reduce each phase current [10]. However, along with the increase of phase number, the number of power devices in converter is also multiplied, then the volume and cost of converter will increase. The novel converter topologies with high performance and less power devices simultaneously are one of the optimization directions of multiphase SRM drive system. In [11] and [12], a six-phase m-switch converter is studied, this converter topology requires only six switches, each phase shares one half bridge arm with the previous phase

and another half bridge arm with the next phase. In [13] and [14], split-phase converter and three-phase full bridge converter are improved to novel structures and be applied to drive multiphase SRM.

An N+2 converter topology has been proposed in reference [15], which is derived from the split-phase topology and uses two switch devices instead of midpoint capacitors to clamp the midpoint voltage. Compared with an N-phase AHB converter, N-2 switch devices and N power diodes can be saved in this converter. In [16], the midpoint current of the N+2 converter is analysed. The variation rule of midpoint current under different control parameters and fault states is summarized. In [17], an optimal control strategy is proposed to reduce torque ripple and improve efficiency by controlling the midpoint current waveform.

The converter topologies mentioned above can effectively reduce the amount of power devices in multiphase converters. However, in these topologies, power devices should be shared by more than one phase, then the independence and fault tolerance of each phase is reduced, the fault diagnosis process could become complicated.

The optimization of SRM fault diagnosis scheme mainly focuses on improving reliability, reducing detection devices, and simplify diagnostic process [18]. Switch devices are the most vulnerable part in the converter, so most of the fault diagnosis scheme for converters focus on switch devices [19].

In [20], an online diagnosis scheme for transistor faults based on two current measurement methods is proposed. The wires of one bridge arm pass through a current sensor three times, according to the change of the measured current the faulty devices can be located. In [21], fault diagnosis is also realized by changing the wiring to make wires pass through one current sensor multiple times. In [22], the current sensor is installed on the excitation circuit and the demagnetization circuit respectively, two fault diagnosis schemes for three-phase AHB converter is proposed, and the fault characteristics are extracted by calculating the difference of the measured current signals. In [23], a current reconstruction scheme is proposed and applied to a four-phase SRM. The phase currents can be reconstructed with only two sensors regardless of the number of phases. In [24], high-frequency signal injection is used to measure the instantaneous value of phase current, real-time fault identification and broken transistors localization could be implemented.

The fault diagnosis schemes that directly detect current or voltage signals often has the advantages of high reliability and easy to realize online diagnosis, but it also has the disadvantages of modifying circuit structure and long diagnosis time. Hence, in some fault diagnosis schemes, mathematical transformations, including spectrum analysis, wavelet packet analysis, Kalman filter, are applied to the measured signals first, and then fault characteristic is extracted [25]. In [26], FFT algorithm is used to perform spectrum analysis on DC bus current, open-circuit fault diagnosis and faulty devices location is implemented. In [27], the wavelet packet decomposition algorithm is applied to the DC bus currents
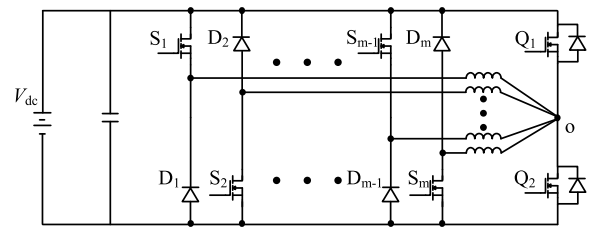


**FIGURE 1.** The topological structure of N+2 converter.

for fault diagnosis, the discrete degree of the wavelet packet node energy is chosen as the fault coefficient. In [28], power converter supply current is analyzed, and the fault is detected when the measured amplitude of the DC bus current differs from its expected amplitude, assuming normal operating conditions. In [29], the presented technique uses the phase currents only, and the algorithm is based on the calculation of average quantities.

In this paper, the N+2 power converter mentioned in [15], [16], and [17] is studied, a fault diagnosis scheme based on spectrum analysis of its midpoint current is proposed. In section II, the typical operation modes and midpoint current characteristics of the N+2 converter under intact condition are introduced. In section III, the open-circuit faults of N+2 converters are classified into four cases, and a new fault diagnosis scheme is proposed based on the variation of the midpoint current spectrum under different fault cases. In section IV, the effectiveness of the proposed fault diagnosis scheme is verified by simulation, different speed and control angle is tested. The method of fault phase location is also described. In section V, the proposed fault diagnosis method is verified by experiment, and the section VI summarizes the whole paper.

## II. THE N+2 CONVERTER AND MIDPOINT CURRENT

The structure of the N+2 converter is shown in Fig.1. The 'N' represents the phases number of SRM. When phases number is even, the number of upper bridge arms and lower bridge arms is equal. The current input terminal of odd phase winding is connected to the upper bridge arm, and the current output terminal of even phase winding is connected to the lower bridge arm. The even phases are opposite to the odd phases. A midpoint bridge arm is connected to the common midpoint for all phase winding.

### A. OPERATION MODES OF N+2 CONVERTER

Fig. 2 (a) and (b) shows four operation modes of the upper bridge arm taking phase A as an example.

Mode 1: Phase switch $S_1$ and the lower switch $Q_2$ of midpoint bridge arm conduction, the current path is shown in the line ① in Fig. 2 (a), the terminal voltage of phase A is $V_{dc}$.

Mode 2: $S_1$ conduction, the current path through the diode inverse-parallel with $Q_1$ which is shown in the line ② in Fig. 2 (a), and the terminal voltage of phase A is 0.
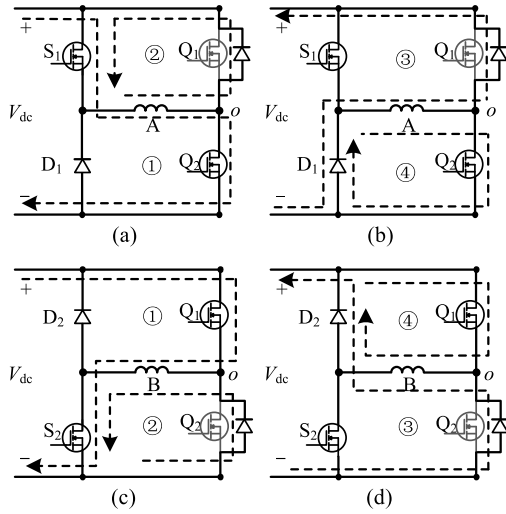
**FIGURE 2. Typical operation modes of phase A and B. (a) Switch device of phase A conduction. (b) Switch device of phase A cut-off. (c) Switch device of phase B conduction. (d) Switch device of phase B cut-off.**

Mode 3: $S_1$ cut-off, the current path through the diode inverse-parallel with $Q_1$ which is shown in the line ③ in Fig. 2 (b). In this mode, phase A is demagnetizing and the terminal voltage of phase A is $-V_{dc}$.

Mode 4: $S_1$ cut-off and $Q_2$ conduction, the current path is shown in the line ④ in Fig. 2 (b), the terminal voltage of phase A is 0.

$Q_1$ and $Q_2$ are set as complementary conduction with a duty cycle of 0.5. When $S_1$ is conduction, in one PWM period of the midpoint switches, the following equation can be obtained:

$$\psi_A = \int_t^{t+T'/2}(V_{dc} - i_A R)\mathrm{d}t + \int_{t+T'/2}^{t+T'}(-i_A R)\mathrm{d}t$$
$$= \int_t^{t+T'}(V_{dc}/2 - i_A R)\mathrm{d}t \qquad (1)$$

where $T'$, $\psi_A$, $i_A$ and $R$ represent PWM period of the midpoint switches, flux-linkage value and current value of phase A, winding resistance respectively.

After reduction, equation (2) can be obtained:

$$\frac{\mathrm{d}\psi_A}{\mathrm{d}t} + iR = V_{dc}/2 \qquad (2)$$

Similarly, when $S_1$ is cut-off, equation (3) can be obtained:

$$\frac{\mathrm{d}\psi}{\mathrm{d}t} + iR = -V_{dc}/2 \qquad (3)$$

Fig. 2 (c) and (d) shows four operation modes of the lower bridge arm taking phase B as an example.

It can also be concluded that the terminal voltage of phase B equivalent to $V_{dc}/2$ when $S_2$ is conduction, and the terminal voltage equivalent to $-V_{dc}/2$ when $S_2$ is cut-off.

To sum up, the effect of N+2 converter can be regarded as an AHB converter with $V_{dc}/2$ bus voltage when the higher harmonics are ignored.
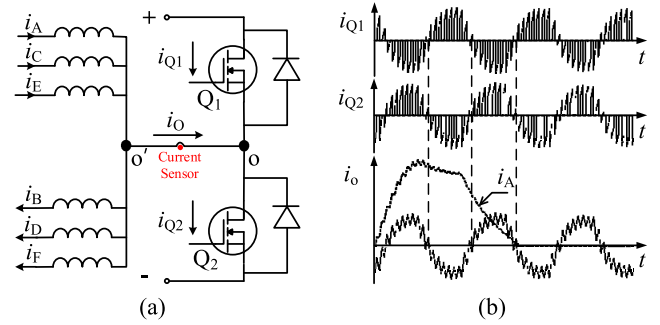


**FIGURE 3. Schematic diagram of midpoint current. (a) Definition of midpoint current $i_o$. (b) Sequence of $i_{Q1}$, $i_{Q2}$, $i_A$, $i_o$.**

## B. THE CHARACTERISTICS OF MIDPOINT CURRENT

For measurement and analysis, the common midpoint $\mathbf{o'}$ of all phase windings is separated from the midpoint $\mathbf{o}$ of the shared bridge arm, the positive direction of $i_o$ flows from $\mathbf{o'}$ to $\mathbf{o}$. As shown in Fig. 3(a), the current sensor is also installed.

The relationship between $i_o$ and the current of each phase can be written as equation (4):

$$i_o = i_A + i_C + i_E - i_B - i_D - i_F \qquad (4)$$

In the equation, $i_A$ to $i_F$ represent the instantaneous value of the phase currents. When the sum of the odd phase current approaches the sum of the even phase current, $i_o$ could be smaller. That is to say, the current stress on the midpoint switches could be lower.

The current equation of the midpoint switches can be written as:

$$i_{Q1} = (-i_A - i_C - i_E) \cdot \bar{S}_{Q2} + (i_B + i_D + i_F) \cdot S_{Q1} \quad (5)$$
$$i_{Q2} = (i_A + i_C + i_E) \cdot S_{Q2} + (-i_B - i_D - i_F) \cdot \bar{S}_{Q1} \quad (6)$$

where $i_{Q1}$ and $i_{Q2}$ represent the current flowing through switch $Q_1$ and $Q_2$ respectively, $S_{Q1}$ and $S_{Q2}$ are the Boolean Function that represents the switching state of $Q_1$ and $Q_2$. When $i_{Q1}$ and $i_{Q2}$ are greater than zero, current flows through the switch devices, and when $i_{Q1}$ and $i_{Q2}$ are less than zero, current flows through the reverse parallel diodes. Combine equations (4), (5) and (6), equation (7) can be obtained:

$$i_o = -i_{Q1} + i_{Q2} \qquad (7)$$

Fig. 6 (b) shows a diagram of $i_{Q1}$, $i_{Q2}$, $i_o$, and $i_A$, $i_{Q1}$ and $i_{Q2}$ is discontinuous and bipolar. On the other hand, the phase current is periodic, so the midpoint current should also be periodic. For an N phases SRM, the frequency of $i_o$ should be N/2 times of the phase current.

## III. FAULT DIAGNOSIS SCHEME

The simulation model of six-phase SRM is established in MATLAB-Simulink, and the parameters of the prototype are shown in Table 1. The midpoint current waveform is analysed, when speed $n$ is 1200r/min, turn-on angle $\theta_{on} = -4°$ (the position of minimum inductor is $0°$) and conduction width $\theta_{wid}$ is equal $12°$.

**TABLE 1.** Parameters of the motor.

| Parameter | Value |
|---|---|
| Stator pole number | 12 |
| Rotor pole number | 10 |
| Stator outer diameter | 155mm |
| Rotor outer diameter | 84mm |
| Gap length | 0.5mm |
| Core length | 65mm |
| Wire turns | 23 |
| Maximum induction | 1.83mH |
| Minimum inductance | 0.35mH |
| Pole arrangement | NSNSNS-SNSNSN |

## A. OPEN-CIRCUIT FAULT IN PHASE SWITCHES

According to the above analysis, in N+2 converter, the open-circuit fault of any phase will lead to the change of $i_o$.

The frequency of phase current can be expressed by speed $n$:

$$f = \frac{np}{60} = \frac{n}{6} \qquad (8)$$

where $f$ is the frequency of phase current, $p$ is the number of rotor poles which is equal to 10. And the frequency of midpoint current $i_o$ is three times that of phase current.

The midpoint current is decomposed by FFT algorithm and $f$ is set as fundamental frequency. The obtained spectrum is shown in Fig. 4.

In the spectrum of $i_o$, the DC component and the fundamental frequency component are very small, only the third harmonic component has a large amplitude. When the open-circuit fault occurs in phase switches, according to the phase current sequence of the faulty phases, there are four fault cases can be analysed.

Case 1: Open-circuit faults occur in only one bridge arm. Then the midpoint current is no longer symmetrical, and the amplitude of DC component, fundamental frequency component and second harmonic component in the spectrum increases greatly. Taking phase A as the example, when the open-circuit fault occurs, the spectrum is shown in Fig. 5 (a).

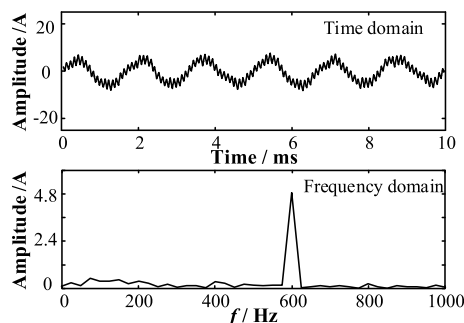Case 2: Open-circuit faults occur in a pair of interval phase bridge arms. Then the DC component, fundamental



**FIGURE 4.** The time domain waveform and frequency spectrum of $i_o$, when N+2 converter is intact.
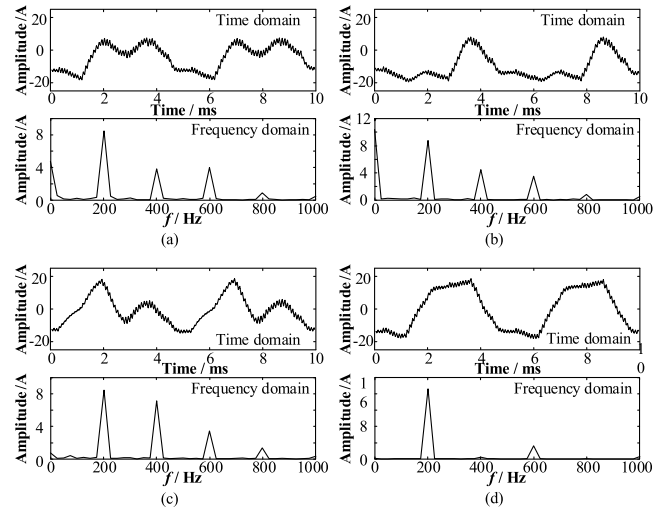


**FIGURE 5.** The time domain waveform and frequency spectrum of $i_o$ when open-circuit fault occurs in phase switches. (a) Open-circuit faults in phase A. (b) Open-circuit faults in phase A and C. (c) Open-circuit faults in phase A and B. (d) Open-circuit faults in phase A and D.

frequency component and second harmonic component of the $i_o$ spectrum will all increase greatly, and the amplitude of the DC component is nearly twice that of single phase bridge arm broken. Taking phase A and C as the example, the frequency spectrum is shown in Fig. 5 (b).

Case 3: Open-circuit faults occur in a pair of adjacent phase bridge arms. Then the amplitude of fundamental frequency component and second harmonic component in spectrum increases obviously, but the DC component is still very small. Taking phase A and B as the example, the frequency spectrum is shown in Fig. 5 (c).

Case 4: Open-circuit faults occur in a pair of complementary phase bridge arms. After the fault occurs, the amplitude of DC component in the frequency spectrum is still small. However, the phase difference between complementary phase is half period, $i_o$ is still symmetrical, so only the amplitude of fundamental frequency component in the fault spectrum increases sharply. Taking phase A and D as the example, the frequency spectrum is shown in Fig. 5 (d).

Since the waveform of phase current will change with the speed and load, it is difficult to take the amplitude of harmonic components as the basis of fault diagnosis.

When the N+2 converter is intact, the third harmonic component amplitude of $i_o$ is greater than zero and change with the load, taking the other spectrum components normalised to the third harmonic component, three spectrum coefficient $\lambda_{03}$, $\lambda_{13}$, and $\lambda_{23}$ could be obtained:

$$\begin{cases} \lambda_{03} = A_0/A_3 \\ \lambda_{13} = A_1/A_3 \\ \lambda_{23} = A_2/A_3 \end{cases} \qquad (9)$$

where $A_0$, $A_1$, $A_2$ and $A_3$ represent the amplitude of dc component, fundamental frequency component, second harmonic component and third harmonic component respectively.

Fig. 5 shows that, the changes of $\lambda_{03}$, $\lambda_{13}$ and $\lambda_{23}$ have obvious differences under different open-circuit fault cases. When the N+2 converter is intact, the values of $\lambda_{03}$, $\lambda_{13}$, and $\lambda_{23}$ are approximately zero. While the values of $\lambda_{13}$ rise sharply when any open-circuit fault case occurs.

In open-circuit faults case 1 and case 2, $\lambda_{03}$ will rise sharply, however the change of $\lambda_{03}$ in open-circuit faults case 3 and case 4 is small. The value of $\lambda_{23}$ in fault case 3 increases greatly, while the value of $\lambda_{23}$ in fault case 4 remains small. According to the variation rule of spectrum coefficient under different open-circuit fault cases, the flow chart for identifying different fault cases shown in Fig. 6 can be obtained.

In Fig.6 $C_1$, $C_2$, $C_3$ and $C_4$ are the fault threshold value for determining the fault cases. In ideal conditions, $\lambda_{13}$ is equal to zero when the N+2 converter is intact. In order to prevent misjudgement, the threshold $C_1$ should be slightly greater than zero. When the actual value of $\lambda_{13}$ is greater than $C_1$, the converter can be judged to have an open-circuit fault.

After the open circuit fault is confirmed, the spectrum coefficient $\lambda_{03}$ is detected, and the value of threshold $C_2$ should also be slightly greater than zero.

If $\lambda_{03} > C_2$, the fault case can be identified as case 1 or case 2. In case 2, the rise of DC component is obviously greater than that of case 1. Therefore, it is easy to distinguish the two fault cases by selecting an appropriate threshold $C_3$ for the second judgment of $\lambda_{03}$.

If $\lambda_{03} < C_2$, the fault case can be determined as case 3 or case 4. The difference of $\lambda_{23}$ between the two fault cases is obvious, and the threshold $C_4$ can be easily selected to achieve accurate fault diagnosis.

### B. OPEN CIRCUIT FAULT IN MIDPOINT SWITCH

Different from the open-circuit fault in phase bridge arms, the open-circuit fault of midpoint switch will directly affect the
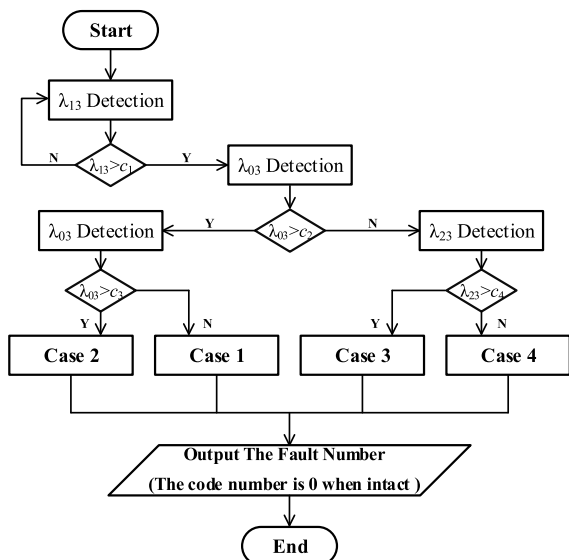


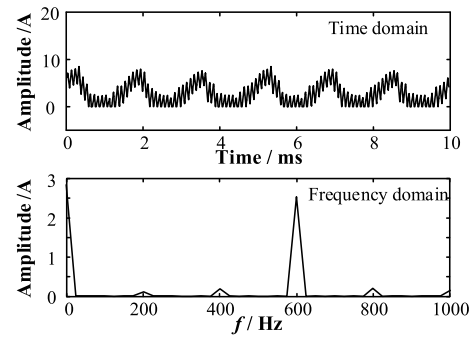**FIGURE 6.** The flow chart for identifying different fault cases.



**FIGURE 7.** The time domain waveform and frequency spectrum of $i_o$ when open-circuit fault occurs in $Q_1$.

circuit of $i_o$. When an open-circuit fault occurs in $Q_1$, the midpoint current can only pass through the reverse parallel diode of $Q_1$, and $i_o$ becomes unipolar. The frequency spectrum is shown in Fig. 7.

When the open-circuit fault occurs in $Q_1$, only the amplitude of the DC component increases greatly, and the amplitude of the third harmonic component decreases to about half of that in the intact condition. That is, the spectrum coefficient $\lambda_{03}$ increases greatly after the fault occurs, while $\lambda_{13}$ and $\lambda_{23}$ are still approximately zero. Hence, the spectrum feature is unique, and can be used for fault diagnosis.

### IV. SIMULATION ANALYSIS UNDER DIFFERENT WORKING CONDITION

#### A. CHANGE OF CONTROL PARAMETERS

In this subsection, the spectrum coefficients under different control parameters are listed and analysed. The pulse-width modulation (PWM) is adjusted in a PI controller to realise closed-loop control. The PWM signal is superimposed on the control signals of phase switches for controlling the speed when changing the parameters.

Fig. 8 shows the variation of the spectrum coefficients at different speeds when the turn-on angle $\theta_{on} = -4°$ and
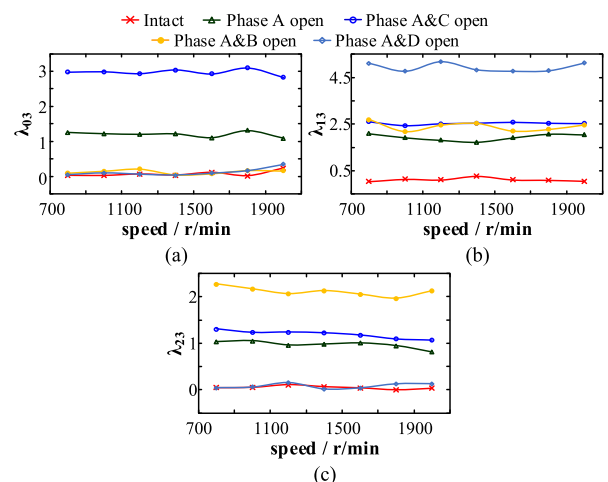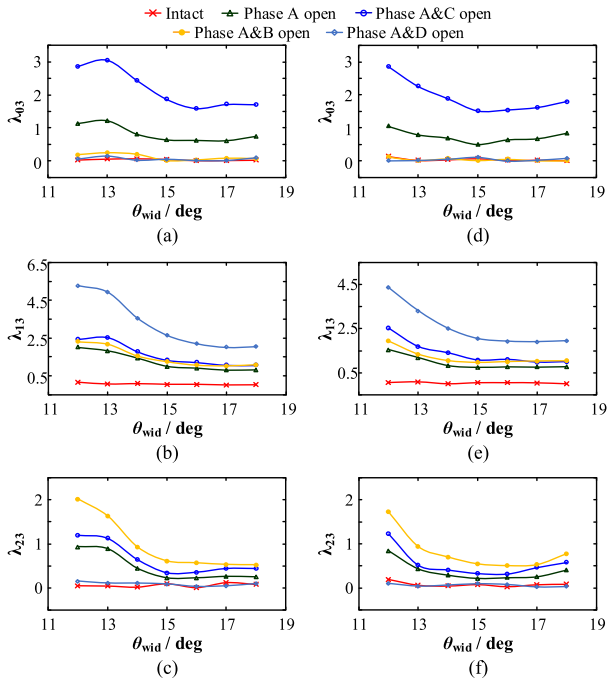


**FIGURE 8.** The spectrum coefficient varies with the speed. (a) $\lambda_{03} = A_0/A_3$. (b) $\lambda_{13} = A_1/A_3$. (c) $\lambda_{23} = A_2/A_3$.
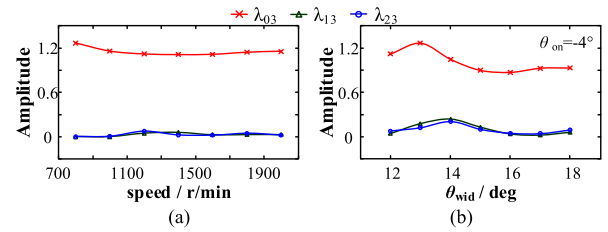
FIGURE 9. The spectrum coefficient varies with $\theta_{\mathrm{wid}}$ while n=1200r/min. (a) $\lambda_{03} = A_0/A_3$, $\theta_{\mathrm{on}} = -4°$. (b) $\lambda_{13} = A_1/A_3$, $\theta_{\mathrm{on}} = -4°$. (c) $\lambda_{23} = A_2/A_3$, $\theta_{\mathrm{on}} = -4°$. (d) $\lambda_{03} = A_0/A_3$, $\theta_{\mathrm{on}} = -2°$. (e) $\lambda_{13} = A_1/A_3$, $\theta_{\mathrm{on}} = -2°$. (f) $\lambda_{23} = A_2/A_3$, $\theta_{\mathrm{on}} = -2°$.

conduction width $\theta_{\mathrm{wid}} = 12°$ unchanged. The coefficient $\lambda_{03}$, $\lambda_{13}$ and $\lambda_{23}$ basically remain unchanged at different speeds, the fault diagnosis scheme has good robustness to speed. Although the speed will fluctuate in real time when one or two phase broken, as long as the fault threshold selected properly, the speed fluctuation does not affect the accuracy of fault diagnosis.

As $\lambda_{03}$, $\lambda_{13}$ and $\lambda_{23}$ will jump from a very small value to a large value in the open-circuit fault cases, the fault threshold $C_1$, $C_2$ and $C_4$ can be easily selected. The selection of fault threshold $C_3$ requires offline simulation in advance and small adjustment according to the load of the motor.

It is pointed out in reference [16] that among the control parameters, $\theta_{\mathrm{wid}}$ has a greatest influence on the characteristics of $i_o$. In Fig. 9 (a), (b), and (c), $\theta_{\mathrm{on}} = -4°$, speed $n = 1200$r/min, when $\theta_{\mathrm{wid}}$ is close to $12°$, the amplitude of $i_o$ is small, so the denominator $A_3$ is very small when calculating the spectrum coefficient. The values of $\lambda_{03}$, $\lambda_{13}$ and $\lambda_{23}$ rising obviously after the open-circuit fault occurrence, and the accuracy of fault diagnosis can be easily guaranteed. However, when $\theta_{\mathrm{wid}}$ is close to $18°$, the amplitude of $i_o$ become larger in the intact state, when the phase bridge arm open-circuit, the rising proportion of spectrum coefficient is smaller, and the selection of fault threshold become difficult and prone to misjudgement. In Fig. 9 (d), (e), and (f) $\theta_{\mathrm{on}}$ changes to $-2°$, the spectrum coefficients also vary with $\theta_{\mathrm{wid}}$ and the change rule just similar to $\theta_{\mathrm{on}} = -4°$.

Fig. 10 (a) shows $\lambda_{03}$, $\lambda_{13}$ and $\lambda_{23}$ vary with the speed when the $Q_1$ has open-circuit fault. Fig. 10 (b) shows the



FIGURE 10. The spectrum coefficient changes when Q1 has open-circuit fault. (a) The spectrum coefficient varies with speed. (b) The spectrum coefficient varies with conduction width.

variation of $\lambda_{03}$, $\lambda_{13}$ and $\lambda_{23}$ with the conduction width. Same with the phase bridge arms broken, when $\theta_{\mathrm{wid}} = 12°$, rising proportion of spectrum coefficient is larger, and when $\theta_{\mathrm{wid}} = 18°$ the rising proportion is smaller. But the numerical difference is not obvious compared with the phase bridge arm fault.

### B. FAULT SWITCHES LOCATION
Based on the above analysis, the spectrum coefficient of midpoint current $i_o$ can determine the fault case, then the fault bridge arms need to be located.

In open-circuit fault case 1, only one phase bridge arm broken. If the broken one is an upper bridge arm, in the interval when the fault phase current should be greater than zero, the negative peak of $i_o$ will rise sharply. If the broken one is a lower bridge arm, the positive peak of $i_o$ will rise sharply. On the other hand, the amplitude of $i_o$ does not change greatly when conduction phase switches are all faultless.

After the frequency spectrum analysis determines fault case, define the fault location threshold $T = A_1 + A_3$ and a upper bridge arm fault location signal $S_{Lu}$:

$$S_{Lu} = \begin{cases} 1 & i_o < -T \\ 0 & i_o \geq -T \end{cases} \tag{10}$$

As shown in Fig. 11 (a), after the open-circuit fault occurs in phase A, the interval of $S_{Lu} = 1$ mostly overlaps the interval of $S_A = 1$ which is the driving signal of the faulty phase. Although it is difficult to ensure the skip edge of $S_{Lu}$ to be completely synchronized with that of $S_A$, it can also ensure that the first jump edge of $S_{Lu}$ is within the interval of $S_A = 1$, then location of broken upper bridge arm can be implemented simply.

Similarly, the lower bridge arm fault location signal $S_{Ld}$ is defined as follow:

$$S_{Ld} = \begin{cases} 1 & i_o > T \\ 0 & i_o \leq T \end{cases} \tag{11}$$

As shown in Fig. 11 (b), most of the interval of $S_{Ld} = 1$ overlapped with the interval of $S_B = 1$ after the open circuit fault occurred in phase B.

Hence, the complete fault diagnosis process is as follow.

① The fault type can be determined by spectral coefficient variation.
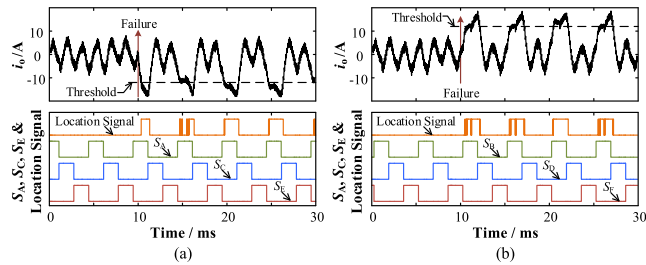
**FIGURE 11.** Location of broken bridge arm when single phase failure. (a) An upper bridge arm broken. (b) A lower bridge arm broken.
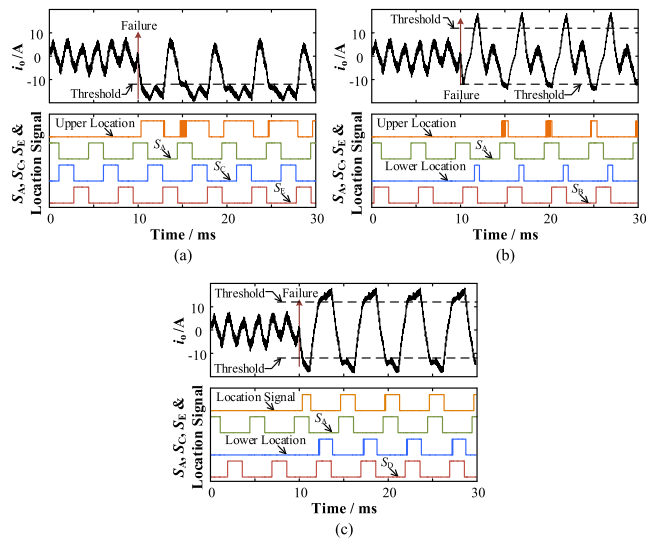


**FIGURE 12.** Location of broken bridge arm when two phases failure. (a) Phase A and phase C broken. (b) Phase A and phase B broken. (c) Phase A and phase D broken.

② Measure the current values of $A_1$ and $A_3$ to determine the fault locating threshold.

③ Compare $T$ and $-T$ with $i_o$ respectively.

④ If the upper bridge arm fault location signal $S_{Lu}$ jumps to high level, detect $S_A$, $S_C$ and $S_E$ and the phase whose driving signal is high level is the fault phase. If $S_{Ld}$ jumps to high level, detect $S_B$, $S_D$ and $S_F$ to confirm the fault phase.

Fig. 12 shows the sequential relationship between fault location signals and driving signals in three two-phase fault cases. Similarly, select the fault locating threshold $T = A_1 + A_3$.

As shown in Fig. 12 (a), if the upper bridge arms of phase A and phase C broken simultaneously, the high level region of the fault location signal must be wider than single-phase broken and overlap with the drive signal of non-fault phase. While, in fault cases 3 and 4, which is corresponding to Fig. 12 (b) and (c), both fault location signals $S_{Lu}$ and $S_{Ld}$ have high level region. Fig. 13 shows the flowchart of the fault phases location process. Due to space limitation, some similar branches are omitted. Before locating the fault bridge arms, the fault code number has been determined, then rising edge of the fault locating signal needs to be detected.
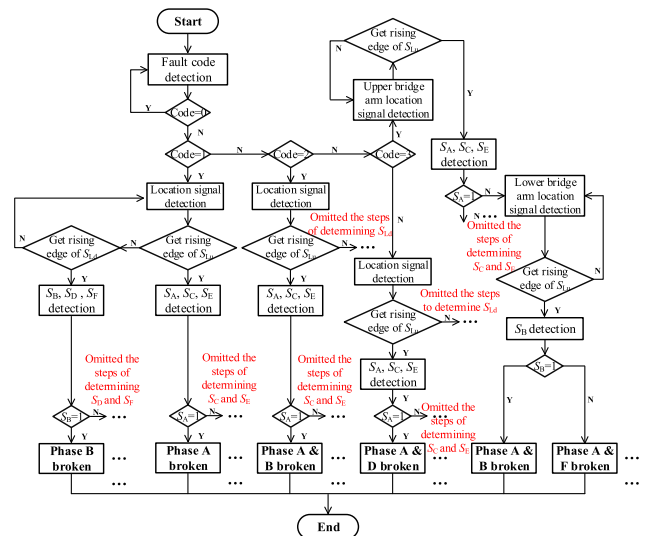


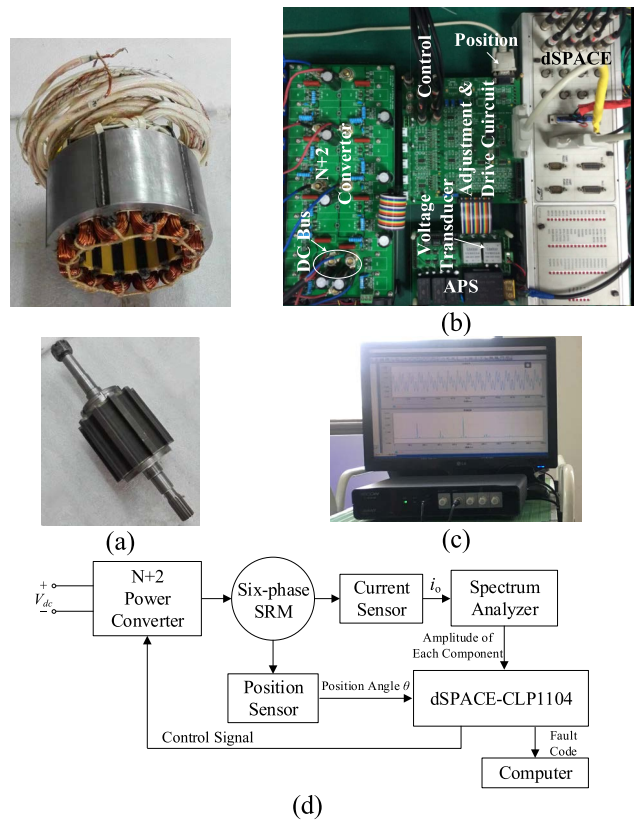**FIGURE 13.** The flow chart for fault phase location.



**FIGURE 14.** The experimental platform. (a) The picture of the stator and rotor. (b) The picture of the controller and converter. (c) The picture of the spectrum analyzer and upper computer. (d) The system block diagram.

Since the fault location method need to get the rising edge of the fault location signal, the location process may take one or two current cycles. Hence, the slow detection speed is the shortcoming of the proposed fault diagnosis scheme that needs to be improved.
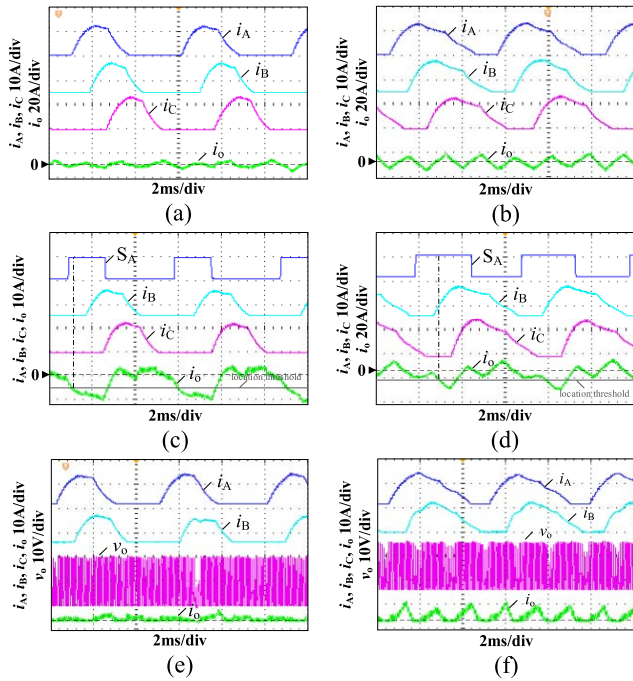
**FIGURE 15.** The time domain waveform of N+2 converter when n=1200r/min and $\theta_{on} = -4°$. (a) Intact condition, $\theta_{wid} = 12°$. (b) Intact condition, $\theta_{wid} = 18°$. (c) The $S_1$ open-circuit, $\theta_{wid} = 12°$. (d) The $S_1$ open-circuit, $\theta_{wid} = 18°$. (e) The $Q_1$ open-circuit, $\theta_{wid} = 12°$. (f) The $Q_1$ open-circuit, $\theta_{wid} = 18°$.



**FIGURE 16.** The spectrum of $i_o$. (a) Intact condition. (b) Open-circuit fault in phase A. (c) Open-circuit fault in phase A and C. (d) Open-circuit fault in phase A and B. (e) Open-circuit fault in phase A and D.

For the midpoint bridge arm open-circuit fault, after one of the midpoint switch broken, $i_o$ will become unipolar. If the open-circuit fault occurs in $Q_1$, $i_o$ will always be greater than zero, while when $Q_2$ is broken, $i_o$ will always be less than zero. Therefore, after judging that the fault bridge arm is the midpoint bridge arm, the fault switch can be determined by detecting the polarity of midpoint current directly.

For a six-phase SRM using other power converter topologies, equation (4) can also be used to construct a virtual $i_o$. Then similar fault diagnosis scheme for open-circuit fault could be used. However, modifying the circuit structure or adding more current sensors is necessary.
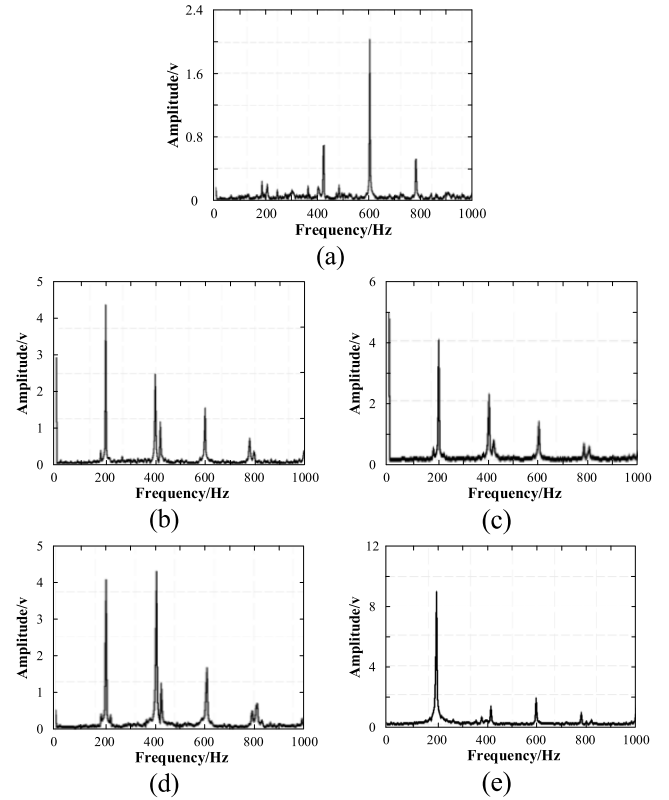
## V. EXPERIMENTAL VERIFICATION
The experimental platform employed in this paper is mainly composed of three parts: ① six-phase 12/10 SRM which is shown in Fig.14 (a); ② N+2 power converter and its controller which is shown in Fig.14 (b); ③ spectrum analyzer and upper computer which is shown in Fig.14 (c). And the system block diagram is shown in Fig. 14 (d).

### A. THE TIME DOMAIN WAVEFORM
Fig.15 shows the time-domain waveform of N+2 power converter in intact condition, open-circuit fault of $S_1$, open-circuit fault of $Q_1$, $n$ is set to 1200r/min, and $\theta_{on} = -4°$.

In Fig.15 (a) and (b), the power converter is intact, and the conduction width is set to 12° and 18° respectively. Consistent with the theoretical analysis, the midpoint current

is periodic when the converter is intact, and the period is three times of the phase current period.

When $\theta_{wid} = 12°$, the amplitude of $i_o$ is small, and when $\theta_{wid} = 18°$, the amplitude of $i_o$ is large.

In Fig.15 (c) and (d), the phase switch $S_1$ is cut-off, and the negative peak value of $i_o$ increases substantially. The gray line in the figure shows the fault location threshold calculated based on spectrum analysis. It can be seen that where $i_o$ is less than the fault threshold the control signal $S_A$ is high level. In Fig.15 (e) and (f), the midpoint switch $S_1$ is cut-off, and $i_o$ becomes unipolar.

### B. EXPERIMENTAL OF HIGH SPEED STATE
In Fig. 16, the spectrum of $i_o$ in different working condition is shown. Similarly, $n$ is set to 1200r/min, and $\theta_{on} = -4°$. And the phase current frequency is set to the fundamental frequency.

In Fig. 16 (a), similar to the simulation results, when the converter is intact, the amplitude of the third harmonic component is the largest, while the amplitude of the DC component, the fundamental frequency component and the second harmonic component are small.

Fig. 16 (b), (c), (d), (e) shows the spectrum of four different fault cases.

In Fig. 16 (b), $S_1$ is open-circuit, the DC component, fundamental frequency component and second harmonic
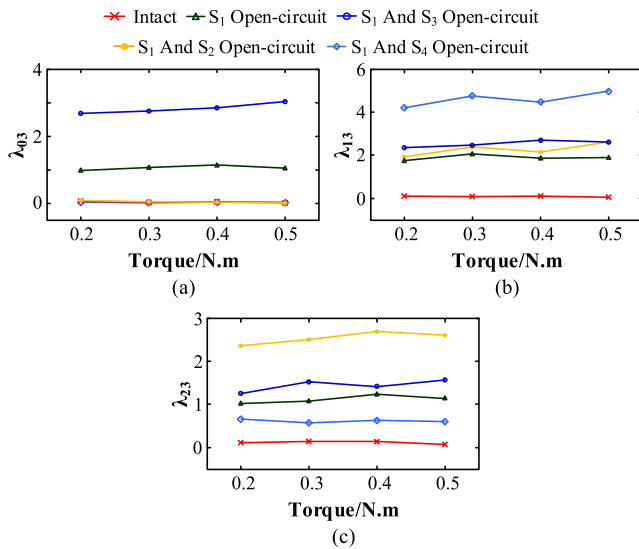
**FIGURE 17.** The spectrum coefficient varies with the load torque. (a) $\lambda_{03} = A_0/A_3$. (b) $\lambda_{13} = A_1/A_3$. (c) $\lambda_{23} = A_2/A_3$.

component all rise obviously. In Fig. 16 (c), both $S_1$ and $S_3$ are open-circuit, the amplitude of DC component is larger than that when only $S_1$ is open-circuit. In Fig. 16 (d), both $S_1$ and $S_2$ are open-circuit, the fundamental frequency component and the second harmonic component rise obviously and the DC component is still very small. In Fig. 16 (e), both $S_1$ and $S_4$ are open-circuit, only the fundamental component of the spectrum increases significantly. In summary, the experimental results are consistent with the theoretical and simulation conclusions.

Fig. 17 shows the spectrum coefficient calculated from the measured spectrum data of $i_o$. Each data point corresponds to a different output torque. During the experiment, the $V_{dc}$ is adjusted to ensure the speed remain unchanged. The values of spectrum coefficient are in good agreement with the simulation results, and the variation rules are obvious under different fault cases. Furthermore, the coefficient $\lambda_{03}$, $\lambda_{13}$ and $\lambda_{23}$ has good stability under different load torque, which indicates that the fault diagnosis scheme has good robustness.

## VI. CONCLUSION

In this paper, open-circuit faults in a six-phase N+2 converter for SRM drives are analyzed and a new fault diagnosis method is proposed. Only one current sensor is needed to detect the midpoint current, and a FFT algorithm is employed in spectrum analysis, the phase current frequency is taken as the fundamental frequency. According to the sequence relationship of the fault phases, the phase bridge arm faults can be divided into four cases. And there is one fault case of midpoint bridge arm fault. Simulation and experiment show that under five fault cases, the frequency spectrum variation of the midpoint current is significantly different. The DC component, fundamental component and second harmonic component are regarded as numerators, the third harmonic

component is taken as the denominator, three spectrum coefficients can be obtained and be used as a fault characteristic.

When the fault case is determined as phase bridge arm fault, the sum of the fundamental frequency component and the third harmonic component in the spectrum is taken as the fault location threshold. If the open-circuit fault occurs at the midpoint bridge arm, detecting the polarity of the midpoint current can locate the faulty switch. The complete process of fault diagnosis and location is described. Simulation and experiments have proved that, the extracted fault characteristic has excellent robustness.

The proposed fault diagnosis method is simpler. It only needs to measure and analyze the midpoint point current without modifying the circuit structure, and there are few additional measuring devices. This work could help improve the application prospect of multiphase SRM and novel structure power converter with less power device.

## COMPETING INTERESTS
The authors declare that they have no competing interests.

## REFERENCES

[1] A. Ghaffarpour and M. Mirsalim, "Split-tooth double-rotor permanent magnet switched reluctance motor," *IEEE Trans. Transport. Electrific.*, vol. 8, no. 2, pp. 2400–2411, Jun. 2022.

[2] F. P. Scalcon, G. Fang, C. J. V. Filho, H. A. Grundling, R. P. Vieira, and B. Nahid-Mobarakeh, "A review on switched reluctance generators in wind power applications: Fundamentals, control and future trends," *IEEE Access*, vol. 10, pp. 69412–69427, 2022.

[3] K. Diao, X. Sun, G. Bramerdorfer, Y. Cai, G. Lei, and L. Chen, "Design optimization of switched reluctance machines for performance and reliability enhancements: A review," *Renew. Sustain. Energy Rev.*, vol. 168, Oct. 2022, Art. no. 112785.

[4] B. Jing, X. Dang, Z. Liu, and S. Long, "Torque ripple suppression of switched reluctance motor based on fuzzy indirect instant torque control," *IEEE Access*, vol. 10, pp. 75472–75481, 2022.

[5] X. Sun, L. Feng, Z. Zhu, G. Lei, K. Diao, Y. Guo, and J. Zhu, "Optimal design of terminal sliding mode controller for direct torque control of SRMs," *IEEE Trans. Transport. Electrific.*, vol. 8, no. 1, pp. 1445–1453, Mar. 2022.

[6] L. Feng, X. Sun, X. Tian, and K. Diao, "Direct torque control with variable flux for an SRM based on hybrid optimization algorithm," *IEEE Trans. Power Electron.*, vol. 37, no. 6, pp. 6688–6697, Jun. 2022.

[7] M. Iida, K. Umetani, T. Kusumi, M. Ishihara, and E. Hiraki, "Sinusoidal-flux reluctance machine driven with three-phase inverter for improving power density with reduced torque and input current ripples," in *Proc. 23rd Eur. Conf. Power Electron. Appl. (EPE ECCE Europe)*, Sep. 2021, p. 10.

[8] A. K. Rana and A. V. R. Teja, "Fast discharging (N+1) switch converter with regenerative flyback operation for N-phase SRM drives," *IEEE Trans. Power Electron.*, vol. 37, no. 7, pp. 8359–8368, Jul. 2022.

[9] V. Fernao Pires, A. Cordeiro, D. Foito, A. J. Pires, J. Martins, and H. Chen, "A multilevel fault-tolerant power converter for a switched reluctance machine drive," *IEEE Access*, vol. 8, pp. 21917–21931, 2020.

[10] X. Deng, B. Mecrow, R. Martin, and S. Gadoue, "Effects of winding connection on performance of a six-phase switched reluctance machine," *IEEE Trans. Energy Convers.*, vol. 33, no. 1, pp. 166–178, Mar. 2018.

[11] X. Deng, B. Mecrow, H. Wu, and R. Martin, "Design and development of low torque ripple variable-speed drive system with six-phase switched reluctance motors," *IEEE Trans. Energy Convers.*, vol. 33, no. 1, pp. 420–429, Mar. 2018.

[12] Y. Hu, T. Wang, and W. Ding, "Performance evaluation on a novel power converter with minimum number of switches for a six-phase switched reluctance motor," *IEEE Trans. Ind. Electron.*, vol. 66, no. 3, pp. 1693–1702, Mar. 2019.

[13] Y. Tang, Y. He, F. Wang, H. Xie, J. Rodriguez, and R. Kennel, "A drive topology for high-speed SRM with bidirectional energy flow and fast demagnetization voltage," *IEEE Trans. Ind. Electron.*, vol. 68, no. 10, pp. 9242–9253, Oct. 2021.

[14] R. Martin, J. D. Widmer, B. C. Mecrow, M. Kimiabeigi, A. Mebarki, and N. L. Brown, "Electromagnetic considerations for a six-phase switched reluctance motor driven by a three-phase inverter," *IEEE Trans. Ind. Appl.*, vol. 52, no. 5, pp. 3783–3791, Sep. 2016.

[15] S. Dai, C. Zhou, and C. Liu, "DC-biased SPWM voltage control for six-phase switched reluctance motor drive based on N+2 power electronic converter," in *Proc. 41st Annu. Conf. IEEE Ind. Electron. Soc.*, Yokohama, Japan, Nov. 2015, pp. 25–30.

[16] M. Guan, C. Liu, S. Han, and X. Sun, "Analysis of midpoint current characteristics for novel six-phase N+2 power converter in different working condition," *IEEE Access*, vol. 8, pp. 105104–105117, 2020.

[17] T. Kusumi and E. Hiraki, "Six-phase switched reluctance motors with small torque ripple, radial force ripple, DC current ripple, copper loss, and number of switches," in *Proc. IEEE Energy Convers. Congr. Expo. (ECCE)*, Oct. 2021, pp. 4306–4312.

[18] C. Gan, Y. Chen, R. H. Qu, Z. Y. Yu, W. B. Kong, and Y. H. Hu, "An overview of fault-diagnosis and fault-tolerance techniques for switched reluctance machine systems," *IEEE Access*, vol. 7, pp. 174822–174838, 2019.

[19] S. Xu, H. Chen, J. Yang, and F. Dong, "Performance evaluation and reliability enhancement of switched reluctance drive system by a novel integrated power converter," *IEEE Trans. Power Electron.*, vol. 34, no. 11, pp. 11090–11102, Nov. 2019.

[20] H. Chen, C. Fang, G. Guan, and N. Parspour, "Fault diagnosis for power converter in SRM drives based on current prediction," *IEEE Trans. Ind. Electron.*, vol. 69, no. 12, pp. 13576–13585, Dec. 2022.

[21] G. Han and B. Zhu, "Virtual current coefficients based power transistors fault diagnosis for small power EV-SRM drives," *IEEE Trans. Transport. Electrific.*, vol. 7, no. 4, pp. 2881–2891, Dec. 2021.

[22] H. Chen and S. Lu, "Fault diagnosis digital method for power transistors in power converters of switched reluctance motors," *IEEE Trans. Ind. Electron.*, vol. 60, no. 2, pp. 749–763, Feb. 2013.

[23] W. Peng, J. J. C. Gyselinck, J.-W. Ahn, and D.-H. Lee, "Minimal current sensing strategy for switched reluctance machine control with enhanced fault-detection capability," *IEEE Trans. Ind. Appl.*, vol. 55, no. 4, pp. 3725–3735, Jul./Aug. 2019.

[24] N. Ali, Q. Gao, P. Sovicka, P. Makys, M. Stulrajter, and K. Ma, "Power converter fault detection and isolation using high-frequency voltage injection in switched reluctance motor drives for automotive applications," *IEEE J. Emerg. Sel. Topics Power Electron.*, vol. 10, no. 3, pp. 3395–3408, Jun. 2022.

[25] P. Bogusz, M. Korkosz, and J. Prokop, "Current harmonics analysis as a method of electrical faults diagnostic in switched reluctance motors," in *Proc. IEEE Int. Symp. Diag. Electric Mach., Power Electron. Drives*, Cracow, Poland, Sep. 2007, pp. 426–431.

[26] C. Gan, J. Wu, S. Yang, Y. Hu, W. Cao, and J. Si, "Fault diagnosis scheme for open-circuit faults in switched reluctance motor drives using fast Fourier transform algorithm with bus current detection," *IET Power Electron.*, vol. 9, pp. 20–30, Jan. 2016.

[27] C. Gan, J. Wu, S. Yang, Y. Hu, and W. Cao, "Wavelet packet decomposition-based fault diagnosis scheme for SRM drives with a single current sensor," *IEEE Trans. Energy Convers.*, vol. 31, no. 1, pp. 303–313, Mar. 2016.

[28] N. S. Gameiro and A. J. Marques Cardoso, "A new method for power converter fault diagnosis in SRM drives," *IEEE Trans. Ind. Appl.*, vol. 48, no. 2, pp. 653–662, Mar. 2012.

[29] J. F. Marques, J. O. Estima, N. S. Gameiro, and A. J. M. Cardoso, "A new diagnostic technique for real-time diagnosis of power converter faults in switched reluctance motor drives," *IEEE Trans. Ind. Appl.*, vol. 50, no. 3, pp. 1854–1860, May 2014.

**MINJUN GUAN** received the B.Eng., M.Eng., and Ph.D. degrees in electrical engineering from the Nanjing University of Aeronautics and Astronautics, Nanjing, China, in 2011, 2014, and 2020, respectively. She is currently a Lecturer with the College of Mechanical and Electrical Engineering, Jinling Institute of Technology. Her research interests include high efficiency switched reluctance motor drive systems for automotive, renewable energy, and household appliances, especially the research of novel power converter of multi-phase SRMs.

**CHUANG LIU** was born in Anhui, China, in 1973. He received the B.S. degree in electrical engineering from Yanshan University, Qinhuangdao, China, in 1994, and the M.S. and Ph.D. degrees in electrical engineering from the Nanjing University of Aeronautics and Astronautics, Nanjing, China, in 1997 and 2000, respectively. In 2000, he was a Postdoctoral Researcher with the Nanjing University of Aeronautics and Astronautics, where he joined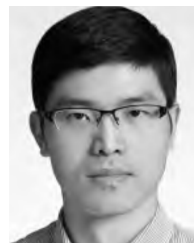 the Department of Electrical Engineering, in 2002. He has been a Professor with the Department of Electrical Engineering, College of Automation Engineering, Nanjing University of Aeronautics and Astronautics, since 2008. His research interests include the permanent-magnet synchronous motors and switched reluctance motors for automotive, renewable energy, and aerospace applications.

**PEILIN LIU** received the B.Eng. degree in automation from the Chengxian College, Southeast University, Nanjing, China, in 2015, and the M.S. degree in electrical engineering from Shanghai Dianji University, Shanghai, China, in 2018. He is currently pursuing the Ph.D. degree in electrical engineering with the Nanjing University of Aeronautics and Astronautics, Nanjing. His research interests include high efficiency switched reluctance motor drive systems for automotive and renewable energy, especially the control strategy of automotive of SRM.

**XIAODONG SUN** (Senior Member, IEEE) received the B.Sc. degree in electrical engineering and the M.Sc. and Ph.D. degrees in control engineering from Jiangsu University, Zhenjiang, China, in 2004, 2008, and 2011, respectively. Since 2004, he has been with Jiangsu University, where he is currently a Professor with the Automotive Engineering Research Institute. From 2014 to 2015, he was a Visiting Professor with the School of Electrical, Mechanical, and Mechatronic Systems, University of Technology Sydney, Sydney, Australia. His current teaching and research interests include electrical machines and drives, drives and control for electric vehicles, and intelligent control. He is the author or coauthor of over 80 refereed technical papers and one book and is the holder of 36 patents in his areas of interests.

● ● ●